RESEARCH ARTICLE | AUGUST 01 2008

Lumped element-based, highly sub-wavelength, negative index metamaterials at UHF frequencies ⊘

Aycan Erentok; Richard W. Ziolkowski; J. A. Nielsen; R. B. Greegor; C. G. Parazzoli; M. H. Tanielian; Steven A. Cummer; Bogdan-Ioan Popa; Thomas Hand; D. C. Vier; S. Schultz

Check for updates

View Online   Export Citation

28 March 2024 06:06:59

Lumped element-based, highly sub-wavelength, negative index metamaterials at UHF frequencies

Aycan Erentok,[1] Richard W. Ziolkowski,[1,a)] J. A. Nielsen,[2] R. B. Greegor,[2] C. G. Parazzoli,[2] M. H. Tanielian,[2] Steven A. Cummer,[3] Bogdan-Ioan Popa,[3] Thomas Hand,[3] D. C. Vier,[4] and S. Schultz[4]

[1]*Department of Electrical and Computer Engineering, University of Arizona, 1230 E. Speedway Blvd., Tucson, Arizona, 85721-0104, USA*
[2]*Boeing Phantom Works, P.O. Box 3999, MC 3W-81 Seattle, Washington 98124-2499, USA*
[3]*Electrical and Computer Engineering, Department P.O. Box 90291, Duke University, Durham, North Carolina 27708, USA*
[4]*Department of Physics, University of California, San Diego, 9500 Gilman Drive, La Jolla, California 92093, USA*

Several lumped element-based epsilon-negative (ENG), mu-negative (MNG), and double-negative (DNG) metamaterial designs have been developed for operation at 400 MHz in the UHF frequency band. The use of lumped elements enabled the creation of highly sub-wavelength unit cells whose overall size was $\lambda_0/d \sim 75$ at 400 MHz. The measured negative index material (NIM) showed an effective real index of refraction $n_{real} = -3.11$ with a total loss that was less than 1 dB/cm. The NIM bandwidth was $>10\%$ in the neighborhood of 400 MHz. © *2008 American Institute of Physics.* [DOI: 10.1063/1.2959377]

I. INTRODUCTION

Metamaterials (MTMs) are artificial media characterized by constitutive parameters whose values, in principle, can be engineered to achieve any specified value—positive or negative. It has been discussed how electromagnetic waves can have counterintuitive properties in their interactions with MTMs, e.g., Refs. 1 and 2, particularly when the permittivities and permeabilities are negative. To date the volumetric MTMs have been realized mainly as composite artificial media formed by periodic arrays of dielectric or metallic inclusions in a host dielectric substrate.[2–8] On the other hand, planar MTMs have been realized successfully with lumped-element-based transmission line structures.[9,10]

We will categorize the materials under discussion in this paper by their constitutive parameters, i.e., by their permittivity ε and permeability μ. If both the permittivity and permeability have positive real parts, as most of the materials in nature do, they will be called "double-positive (DPS)" media. In contrast, if both of these quantities are negative, they will be called "double-negative (DNG)" media. We will also use the term "negative index material (NIM)" in reference to a DNG medium, one having a negative real part of its index of refraction. The materials with one negative constitutive parameter will be called "single-negative (SNG)" media. If the permittivity is negative, these SNG materials will be called "epsilon-negative (ENG)" media. If the permeability is negative, they will be called "mu-negative (MNG)" media.

The increased interest in artificial materials has emerged mainly due to the unusual properties of the DNG MTMs, particularly when they are combined with DPS materials for a variety of applications. Nonetheless, many SNG advantages also have been reported. One application that utilizes either SNG or DNG MTMs is the proposed MTM-based paradigm to achieve efficient electrically small antennas (ESAs).[11–13] For instance, an electrically small ENG or DNG spherical shell surrounding an electrically small dipole antenna can be designed to act as an effective distributed inductor that is properly matched to the capacitance of the electric dipole antenna to form a naturally resonant LC structure, as well as to act as a resistive matching element to the source. Thus, high radiation efficiencies with very good impedance matching between the source and the antenna and, hence, high overall efficiencies can be achieved in such an electrically small radiating system with the assumption that the MTM spherical shell is homogeneous, isotropic, and lossless. The development of such small, efficient, and multiband structures that could fit into a restricted volume while simultaneously accommodating the desired frequencies of operation and high data rates is particularly attractive for wireless communication and sensor network applications. The reciprocal configurations, plane wave scattering from electrically small ENG or DNG MTM-coated spheres, have been shown to exhibit unity normalized total cross sections. By introducing gain media, the effects of losses and dispersion can be controlled in both the radiating[12] and scattering systems.[14] For instance, lasing has been demonstrated at visible wavelengths in an electrically small metal coated nanoparticle.[14]

Many of the cases considered for the efficient ESAs have been in the UHF band (300 MHz–3 GHz). Previous predictions of the radius of the sphere encompassing the entire radiating system have been on the order of 20 mm for 300 MHz, i.e., $r \sim \lambda_0/50$, with shell thicknesses on the order of 10 mm, $t \sim \lambda_0/100$, for an ENG material with $\varepsilon_{real} = -3.0\varepsilon_0$ or a DNG material with $n_{real} = -3.0$ at 300 MHz, where $\lambda_0 = 1.0$ m is the corresponding free-space wave-

length. For a dipole ESA, this requires, for instance, a unit ENG cell size, d, that is a fraction of 10 mm to create an effective ENG medium. The 300 MHz source frequency was originally selected for convenience since the corresponding free-space wavelength is 1.0 m. On the other hand, there are many UHF communication systems that operate at 430 MHz. Consequently, for a compromise in the cell size and frequency of operation, all of the MTM designs considered below deal with a maximum unit cell size of 10 mm at a source frequency of 400 MHz. Thus, at this frequency, the unit cell size is $d \sim \lambda_0/75$. We note that the smaller the unit cell size is, the better the effective medium results should be, i.e., when a unit cell is designed much smaller than a free-space wavelength, a slab that is, for instance, three unit cells deep should have approximately the same effective permittivity and permeability as predicted for the unit cell. Consequently, one would like to be able to design a highly sub-wavelength unit cell to achieve certain material characteristics and have the expectation that a stack of several of these unit cells will produce nearly the same results, i.e., adding one more (artificial) atom to a slab of the material will not change its effective material properties.

In reviewing the physics and the MTM literature, one observes the following: nature gives us ENG materials at high frequencies in very small volumes, e.g., gold and silver at visible wavelengths naturally have negative real parts of their permittivities so that optical MTMs based on gold and silver nanoparticle inclusions share this property. Similarly, it is easy to achieve the MNG materials at low frequencies with small unit cell sizes, i.e., magnetic fields through split loops nicely produce resonances and the desired negative effective permeabilities via Lenz's law. On the other hand, it is difficult with electrically small unit cell sizes to achieve effective ENG properties at low frequencies and effective MNG properties at high frequencies and, hence, effective DNG properties in each of those frequency regimes.

In this paper, we introduce ENG, MNG, and DNG unit cells that have been formed with lumped-element-based volumetric unit cells at the target frequency, 400 MHz, whose maximum length is bounded by $d \sim 10$ mm. The ENG designs introduced here were based on the original proposals described in Refs. 15–17. A nominal target value was selected for the effective index of refraction. In particular, we set out to achieve a NIM behavior at 400 MHz with $n_{real} \approx -3.0$. The lumped-element-based designs, because one can achieve large capacitance or inductance values in very tiny volumes, provide an increase in flexibility in the MTM unit cells while simultaneously being much smaller in size. On the other hand, the introduction of lumped elements in such designs has its own issues, particularly how lossy they are and how well they can be modeled. We note that one of the most important MTM properties of any final design for use in applications, such as the efficient ESAs, is that the resulting unit cells must have small losses. A nominal target value for the experimentally measured loss was thus fixed for our designs to be no greater than 1.0 dB/cm.

Each of the lumped-element-based MTM designs to be discussed in the following sections was fabricated and tested. The fabrication of the resulting NIM structures and a de-
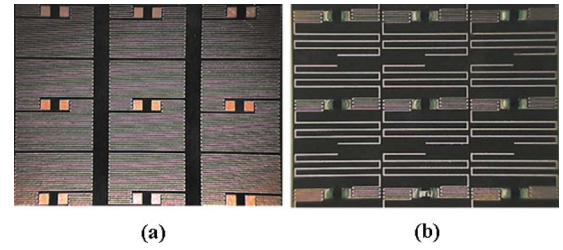

FIG. 1. (Color online) 2D meanderlines integrated with lumped-element inductors for (a) the NIM design 1 unit cell and (b) the NIM design 4 unit cell, both to be discussed in Sec. III.

scription of the measurement procedure are described in Sec. II. The predicted and measured effective material properties of the fabricated NIM structures are discussed in Sec. III. It will be demonstrated that, using the lumped-element-based unit cell approach, ENG, MNG, and DNG unit cells can be achieved in the UHF regime at 400 MHz that are highly sub-wavelength in size ($d \sim \lambda_0/75$), low loss (<1 dB/cm), and produce a NIM behavior with $n_{real}(400 \ \text{MHz}) \approx -3$.

II. NIM SLAB FABRICATION AND MEASUREMENT SETUP

Each of four NIM designs (labeled 1–4 and to be discussed in Sec. III) was fabricated and tested. The designs consisted of three types of unit cell layers: a two-dimensional (2D) meanderline integrated with a lumped-element inductor to realize the ENG portion of the unit cell, which is shown in Fig. 1; a 2D rectangular loop integrated with a lumped-element capacitor to realize the MNG portion of the unit cell, which is shown in Fig. 2; and Rohacell™ layers to provide physical support to the entire NIM unit cell. The presence of the Rohacell™ layers also allows us to control the effective permittivity and permeability values of the proposed NIM structure, as well as the interactions between the ENG and MNG portions of the unit cell. The inductors for the final designs were obtained from Murata, Part No. LQW18ANR47G00, 0603 size, and had the specified value of 470 nH, $\pm 5\%$ at a frequency of 10 MHz. The capacitors were also obtained from Murata, Part No. GQM1885C2A5R6CB010D, and had the specified value of 5.6 pF, ± 0.25 pF at 10 MHz.

All of the boards used to realize the unit cell structures were fabricated on Rogers 5880 Duroid™ material. The boards were 10 mils thick with 0.5 oz. copper (~ 17 μm thick copper layers). The front sides of the boards were etched to achieve the desired pattern of the copper; the back-
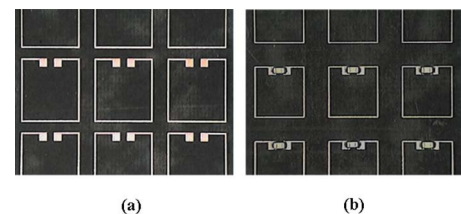

FIG. 2. (Color online) (a) Open 2D rectangular loops and (b) open 2D rectangular loops integrated (closed) with lumped-element capacitors for the MNG portions of the unit cells to be discussed in Sec. III.
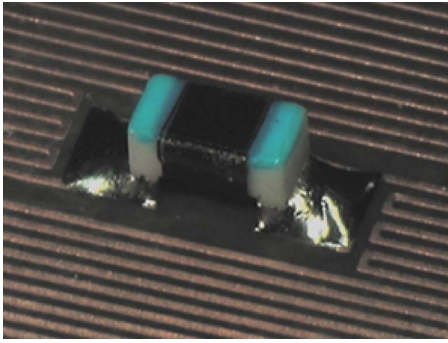
FIG. 3. (Color online) Lumped-element inductor that was hand soldered onto the ENG board

sides of the boards were blanket etched to remove all of the copper. The patterning of the copper layer was performed by Prototron Circuits in Redmond, WA. When the finished boards were received from that vendor, they were laser cut into 3×3 arrays of cells with a CO_2 laser. The fabricated ENG and MNG unit cell designs are shown in Figs. 1 and 2, respectively.

Once the boards were laser cut, the inductors and capacitors (passives) were soldered into place. Figures 3 and 4 show the soldered lumped elements on the fabricated 2D meanderline and the 2D rectangular loop, respectively. On the initial version of the board, the passives were hand soldered into place, as shown in Fig. 3. This method was used solely to expedite the fabrication process. When the second version of the boards was completed, solder stencils were available to use to control the pattern and thickness of the solder paste. Vapor phase technology was then used to reflow the solder. Figure 4 demonstrates that this method allowed us to use less solder and the results were more repeatable than hand soldering. We also considered the use of a solder mask to limit the flow of the solder paste during the reflow process but rejected this idea since the solder mask stays on the board after the reflow process. It was our belief that having the solder mask between the arms of the meanderline would have increased the losses.

After the passives were soldered, the boards were cleaned with isopropyl alcohol to remove any remaining debris from the solder process and the laser cutting. The boards were then assembled into a long slab or "tower" for testing. These slabs were $3 \times 3 \times 15$ mm^3 in size and consisted of
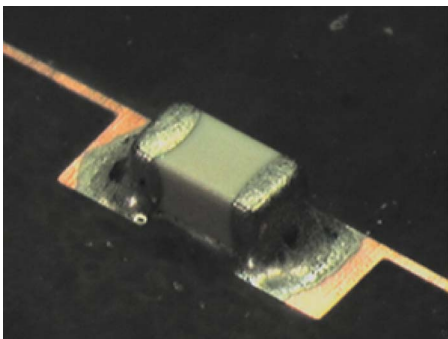

FIG. 4. (Color online) Lumped-element capacitor that was soldered onto the MNG board using stencil reflow
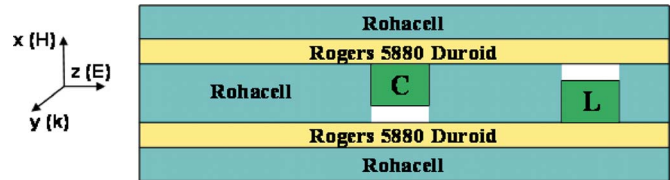

FIG. 5. (Color online) Cross section of the NIM unit cell realizations showing the embedded capacitor (C) and inductor (L) within the Rohacell cutout holes. The polarization (E along z and H along x) and propagation (along y) directions of the electromagnetic wave excitation are indicated.

alternate layers of patterned board material and Rohacell™ spacers. Small holes were cut into the spacers to allow the passives to become "embedded" into the Rohacell™. The assembly method in cross section and photographs of a fabricated NIM design (design 4), including the Rohacell™ spacer with its laser cut holes, are shown in Figs. 5 and 6, respectively.

The assembly of the long slab was done inside an aluminum fixture, which helped to keep the slab squared and which also compressed the spacers to help control the cell thickness. The entire slab was then covered with Top Flite MonoKote®, a heat shrinkable plastic used for covering aviation models. This material does not affect the losses and has been used in many past designs for mechanical stability.[18] The slab was then removed from the fixture.

The UHF MTM slab was designed to be excited by an electromagnetic wave propagating along the y-direction of Fig. 5 with its electric (E) and magnetic (H) fields, respectively, polarized along the z- and x-directions. Since a free-space measurement of the transmission properties of a sample at 400 MHz requires a large sample and a correspondingly large free-space test range, we opted to make the measurement in a UHF waveguide. A two conductor trans-
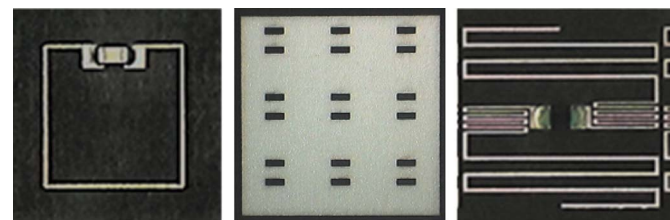
(a) MNG portion   **(b) Rohacell™ spacer**   **(c) ENG portion**
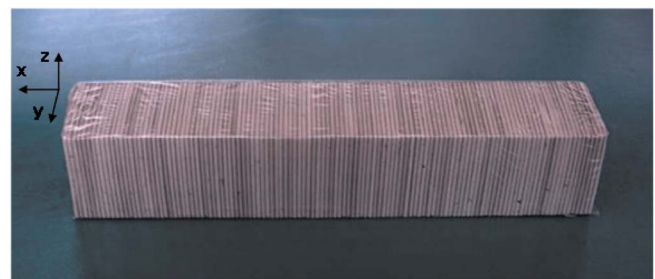
(d) Assembled NIM slab

FIG. 6. (Color online) Photographs of the fabricated NIM design 4: (a) MNG portion of the unit cell, (b) one of the Rohacell™ spacers with the required cutouts, (c) the ENG portion of the unit cell, and (d) the final assembled $3 \times 3 \times 15$ mm^3 NIM slab.
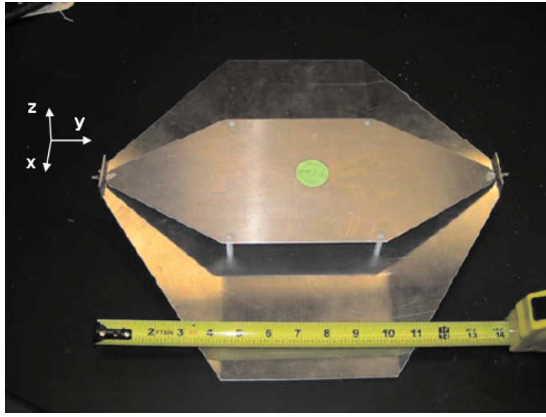
FIG. 7. (Color online) TEM microstrip waveguide used for effective material property measurements.

verse electromagnetic (TEM) microstrip waveguide with a 3 cm plate separation and a 15 cm top plate width was chosen so that the MTM samples described above ($3 \times 3 \times 15$ cm^3) filled the entire cross-sectional area of the waveguide. This TEM microstrip waveguide is shown in Fig. 7. The separation and width of the plates were tapered to maintain a 50 Ω characteristic impedance along the entire length of the waveguide. This open two conductor waveguide has no lower cutoff frequency and is capable of measurements from DC to 5 GHz, where the waveguide finally becomes multimode. Calibration testing with slabs of known permittivity and permeability, such as Rexolite™, yielded good results from 150 MHz to 2 GHz. Closed rectangular waveguides have been used for MTM characterization at higher frequencies,[19,20] but such a waveguide at 400 MHz would require prohibitively large material samples. Since this microstrip waveguide supports a TEM plane wave that is normally incident on the slab under test, the measured complex S-parameters were converted to the effective complex permittivity and permeability of the slab using the approach given in Ref. 21. This approach required reflection and transmission coefficients defined at the incident and transmit boundaries of the slab, and the slab was de-embedded from the waveguide through the S-parameter measurements of a metal plate placed at the same location as the slab. Because the wavelength at 400 MHz is long, the precision required in the placement of this slab was not stringent. Some care had to be taken in the extraction of the effective permittivity and permeability of the MTM slab from the measured S-parameters because of ambiguities introduced by the multivalued arccosine function.[21] However, because the slabs under investigation here were electrically thin and passive [so that the sign of Im(n) was known], these ambiguities were easily resolved. The final result was the measurement of a unique effective permittivity and permeability of the slab under test.

To simulate the behavior of the MTM slab, for instance, with Ansoft's High Frequency Structure Simulator (HFSS), a single unit cell (as detailed in Fig. 8) is placed in a perfect electric conductor (PEC)/perfect magnetic conductor (PMC) waveguide[8] and the S-parameters are calculated. The effective permittivity and permeability of the unit cell are then extracted from the calculated S-parameters in the same manner as for the measurements. The equivalent excitation then is a normally incident plane wave on a slab that is formed as a 2D periodic array of these unit cells. With the coordinate axes indicated in Fig. 8, corresponding to those in Fig. 5, the incident plane wave is modeled as propagating along the y-axis with its electric field polarized along the z-axis and its magnetic field polarized along the x-axis. Note that neither the 2D meanderline nor the 2D rectangular loop touches the PEC/PMC waveguide walls. The modeled NIM unit cell in this study, in contrast to the infinite wire medium, for instance, in Refs. 3–7, is truly finite at these UHF frequencies. It is this required finiteness which causes the difficulty in realizing the desired effective ENG behavior at low frequencies. There is no problem to design an infinite wire medium at these frequencies, but then one is restricted to waveguide applications. Finite designs allow true free-space situations. As shown in Ref. 8, finite metallic inclusions on the order of $\lambda_0/10$ can be used at X-band (10 GHz) frequencies to achieve effective NIM behaviors. However, as demonstrated in Sec. III below, the introduction of the lumped elements into the inclusions facilitates the desired large reduction in cell size and frequency for the present designs.

III. MTM NIM DESIGNS AND MEASUREMENTS

As just noted above, the real challenge for the NIM design at 400 MHz is the design of the ENG portion of the unit cell, i.e., the structure shown in Fig. 8(b). When it is excited by an electric field, the 2D meanderline produces an inductance. However, because the electric field is assumed to be polarized along the z-axis and, hence, is orthogonal to the long arms of the meanderline, and those arms are assumed to be reasonably close together, a capacitance is also generated. Consequently, one can achieve an LC resonance, which in turn leads to the effective negative permittivity values on the high frequency side of that resonance. On the other hand, one could make the meanderline long enough to be self-resonant (half-wavelength). The meanderline captures the electric field of the incident electromagnetic wave and induces current on the sub-wavelength copper traces to produce an electric field that is antiparallel to the incoming wave, and thus overcomes the free-space electric flux to obtain an effective negative permittivity value. The extended 2D copper surface of the meanderline serves as a continuum path for the induced current generated by the electric-field distribution of the incoming wave. The magnitude and the amount of the induced current flow can be adjusted using the meanderline width, length, and the thickness of the copper trace. Another valid explanation for the meanderline behavior can be made if one visualizes each electrically small copper strip as a transmission line terminated in a short circuit. The complex impedance of such a transmission line is inductive, and the whole meanderline can be thought of as a series of inductors that is driven by the incoming electromagnetic wave with its electric field oriented perpendicular to each meanderline.

If one wanted to use only a 2D meanderline for the ENG design at 400 MHz with a $\lambda_0/75$ unit cell size, the real chal-
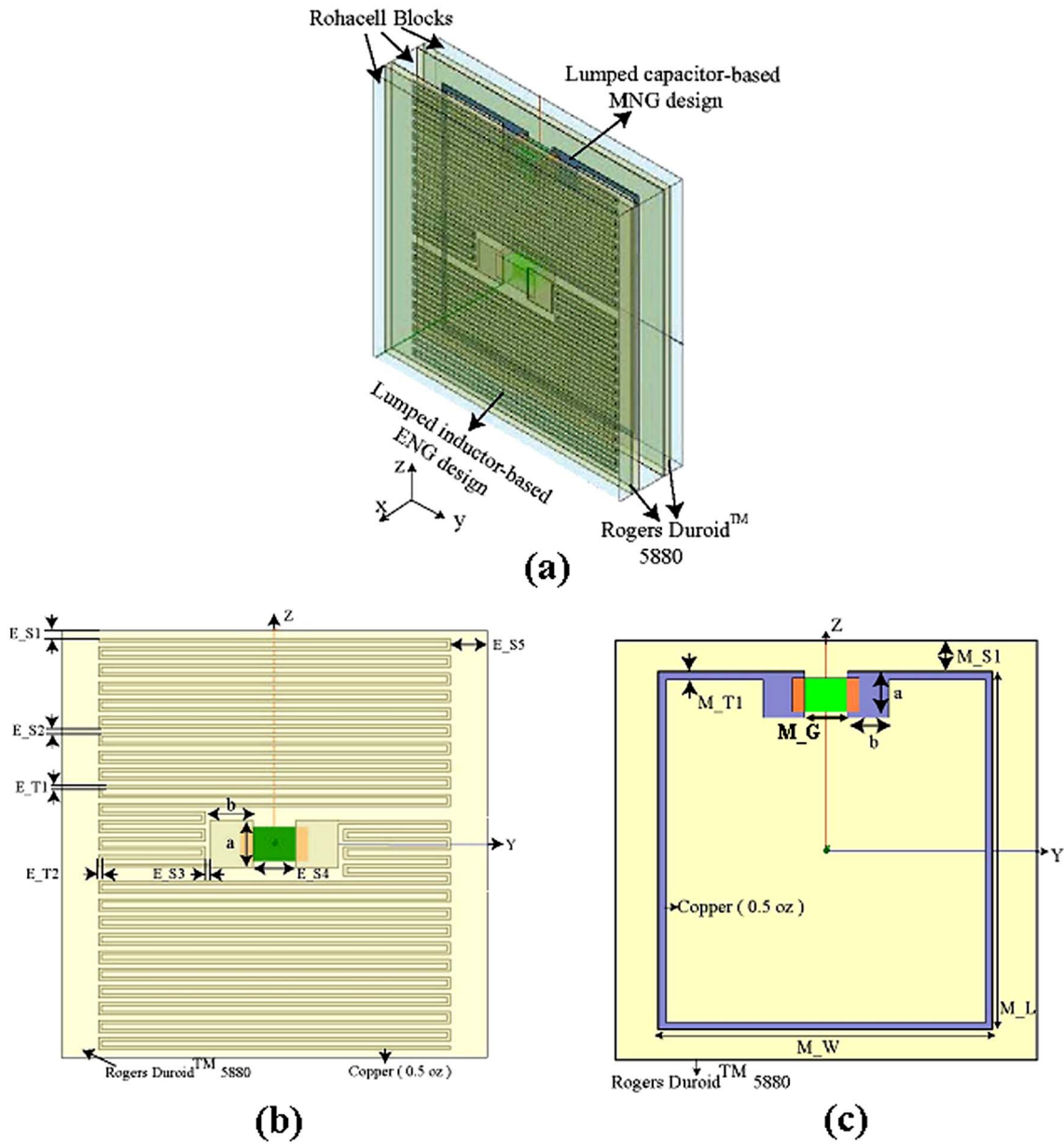
FIG. 8. (Color online) Detailed design specifications of the NIM design 1 unit cell: (a) NIM unit cell, (b) ENG portion of the NIM unit cell based on a 2D meanderline integrated with a lumped-element inductor, and (c) MNG portion of the NIM unit cell based on a 2D rectangular loop integrated with a lumped-element capacitor.

lenge would then be the limitations of the available photolithography fabrication services (how many lines could one fit into a specified finite area) and the conduction losses arising from the extremely thin traces involved. With the fabrication facilities available to us, the minimum copper trace width that could be fabricated to obtain an ENG unit cell with finite copper traces for 0.5 oz. electrodeposited copper is 0.0762 mm. For an equal amount of spacing between the lines, this means one could, in principle, squeeze about 65 traces into the specified $\lambda_0/75$ length. On the other hand, it was found, for instance, in Ref. 15, that while one may obtain negative real parts of the effective permittivity in the neighborhood of the target frequency with only using the 2D meanderline, it is extremely difficult to achieve its resonance well below the target frequency so that the conduction losses in the effective negative permittivity region near the resonance are small.

Moreover, the extremely thin traces favor an increase in the conduction losses since there are very few skin depths of metal present. By integrating the lumped-element inductor with two simple 2D meanderlines, we have been able to transition a majority of the inductance burden from the meanderline to the lumped-element inductor. However, because of limitations on the available values provided by manufacturers, the lumped-element inductors only provide coarse inductance values. The fine tuning of the inductance to achieve a desired resonance frequency must be provided by the 2D meanderline pattern. The lumped-element 2D meanderline then acts more like a loaded electrically small electric antenna, termed an electric molecule in Refs. 22–24. Such a unit cell was shown in Refs. 15–17 to have resonant ENG properties that could achieve the desired low loss and effective negative permittivity values in the UHF regime.

TABLE I. Specifications of the ENG portion of the NIM design 1 unit cell

E_S1 (mm)	E_S2 (mm)	E_S3 (mm)	E_S4 (mm)	E_S5 (mm)	E_T1 (mm)	E_T2 (mm)
0.1828	0.127	0.127	1.0	0.867	0.0762	0.0762

The initial ENG design strategy was based on Rogers 6010 Duroid™ ($\varepsilon_r=10.2$ and $\mu_r=1.0$) material to increase the electrical length of the 2D meanderline and, thus, produce a larger current flow within the ENG unit cell to obtain the desired resonance behavior below the design frequency. Note that the terms $\varepsilon_r=\varepsilon/\varepsilon_0$ and $\mu_r=\mu/\mu_0$ represent permittivity and permeability values relative to vacuum. However, these designs were abandoned in favor of a design series based on Rogers 5880 Duroid™ ($\varepsilon_r=2.2$ and $\mu_r=1.0$) material with 0.5 oz. copper (17 μm thick) and 0.254 mm (10 mils) substrate thickness. Solder pads were introduced explicitly into the design to account for the lumped-element connections. The solder pads had the dimensions: $a\times b=1.1\times1.0$ mm^2. The Rogers 5880 designs were favored because their associated losses were less than for the Rogers 6010 designs, and the Rogers 5880 material was more accessible to us.

For the ENG unit cell it was found, as expected, that the mutual capacitance between the copper strips strictly depends on the distance that separates them. Therefore, increasing the distance between the two copper traces in the 2D meanderline reduces the mutual capacitance and, consequently, the resonance behavior shifts to slightly higher frequencies. Similarly, because the amount of current impacts the magnitude of the electric-field distribution, a reduction in the density of the copper traces in a given area reduces the strength of the resonances. Consequently, as a design rule of thumb, we found that increasing the strip length and decreasing the strip width both provide larger induced currents and, thus, a more emphasized resonance behavior and stronger electric dipole moment.

The MNG unit cell at UHF frequencies was realized using a 2D rectangular loop integrated with a lumped-element capacitor, as shown in Fig. 8(c). The same solder pads used in the ENG unit cell were introduced into the MNG unit cell design. This design represented a lumped-element version of the capacitively loaded loop (CLL) MNG element introduced in Ref. 25, a simplification of the well-known split ring resonator design. The lumped-element capacitor provided an extra capacitance to the rectangular loop structure to further shift the resonance behavior lower in frequency, toward the UHF region, while maintaining a unit cell size that satisfied the initial design goals.

The MNG unit cell was first designed using two oppositely oriented 2D rectangular loops integrated with lumped-element capacitors on the front and back faces of the dielectric substrate to minimize the bianisotropic behavior of these CLL elements. However, it was decided not to implement this MNG unit cell design. First, numerical simulations showed that it was possible to obtain similar NIM results using only one lumped-element-based CLL element in the design if the MNG portion of the unit cell was simply separated from the ENG portion of the unit cell using a Rohacell™ spacer of a particular thickness. Second, it was determined that it would be much easier and less expensive to fabricate one lumped-element-based CLL element in the NIM unit cell rather than two.

The specifications of the NIM design 1 are given in Figs. 8(b) and 8(c); the optimized dimensions are summarized, respectively, in Tables I and II for the ENG and MNG portions of the NIM unit cell. The total thickness along the *x*-axis was 2.542 mm. Therefore, the overall NIM unit cell size was $2.542\times10\times10$ mm^3. The lumped-element capacitor and inductor values used for the NIM design 1 were 5.0 pF and 470 nH, respectively. Note that the lumped elements were embedded into the Rohacell™ layers to decrease the overall thickness of the NIM unit cell.

The initial numerical predictions were performed using the HFSS-only simulations. The lumped elements were modeled using the Ansoft-provided *RLC* boundary condition. Figure 9 shows the values of the real and imaginary components of the effective index of refraction that were extracted from the S_{11} and S_{21} parameters obtained from the NIM design 1 simulations. The real part of the effective index recovered the desired value, i.e., Re$[n(\omega)]=-3.0$ at 400 MHz. The simulated loss at 400 MHz was well below the target value of 1.0 dB/cm.

A slab of this NIM design 1 MTM, which was three unit cells deep, was fabricated and tested. An ENG-only unit cell MTM slab was also fabricated. The ENG-only design was obtained from the NIM design 1 unit cell simply by removing the CLL element portion, i.e., the dimensions that were optimized to achieve the NIM design 1 unit cell and its operating characteristics were used to simulate and fabricate the ENG-only unit cell design. This ENG-only slab also provided an opportunity to test the independence of the ENG and MNG portions of the NIM unit cell design.

Comparisons of the predicted and measured extracted effective relative permittivity and permeability values obtained for the ENG-only MTM slab are given in Fig. 10. The measured resonance frequency for the effective permittivity was 340 MHz, 60 MHz lower than the numerical predictions. The ENG measurement results revealed two important de-

TABLE II. Specifications of the MNG portion and Rohacell™ thickness value of the NIM design 1 unit cell

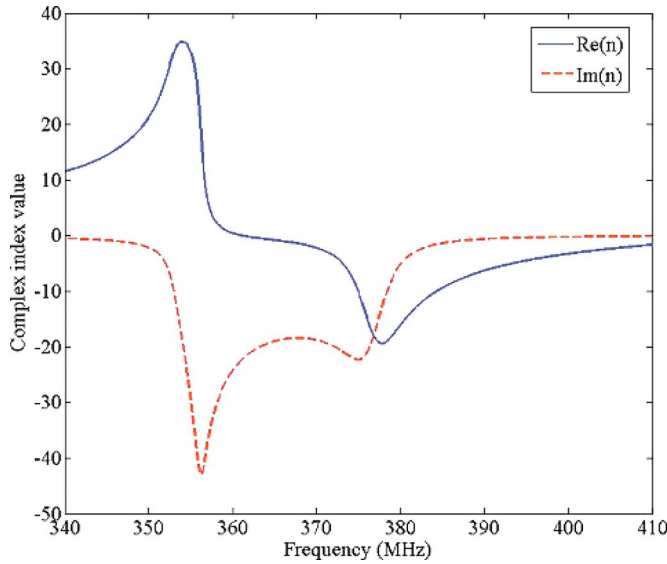| M_W (mm)	M_L (mm)	M_G (mm)	M_T1 (mm)	M_S1 (mm)	Rohacell™ thickness (mm)
7.946	8.546	1.0	0.1778	0.727	1.0

FIG. 9. (Color online) The HFSS-predicted real and imaginary parts of the effective index of refraction for the NIM design 1. These effective values were extracted from the S-parameters predicted with HFSS simulations based on the Ansoft-provided RLC boundary condition.

sign concerns related to the HFSS simulations. First, the resonance frequency predicted with the HFSS simulations, which were based on the HFSS-supplied RLC boundary condition and the fast sweep option, was significantly higher than the measured values. In fact, the observed frequency shift was much larger than the manufacturer's lumped-element tolerance values ($\pm 5\%$). This observation was confirmed further by bounding the simulation results using the lumped-element values based on those tolerance values.

Subsequently, it was concluded that simulations performed with the HFSS RLC boundary condition do not provide a sufficiently accurate prediction of the resonant frequency. Second, the experiments confirmed the simulation results that the ENG and MNG portions of the NIM unit cell are coupled. This means that care must be exercised when attempting to model their behaviors independently and reaching conclusions about how they will combine together to yield the NIM behavior. Their coupling affects the frequency of the resonance in the effective index of refraction associated with the NIM unit cell. An additional, but minor, concern was the predicted extremal values associated with the resonances of the effective permittivity and permeability. As expected, when using lossless lumped elements in the simulations, the predicted resonance extremes were much larger than the measured values since the actual lumped elements are not lossless. While these extremal values have an impact on the frequency locations of the actual negative design values and the zero-crossing values above the resonances, it has been found that the resonance frequencies have a much more significant impact on the final results. It also was found that estimation of a normalization of the extremal values based on comparisons between the simulation and measured values from one experiment carried over to the various modifications of the unit cells which were attempted to achieve the design goals in our final designs. Finally, we note that, to the best of our knowledge, these ENG unit cells
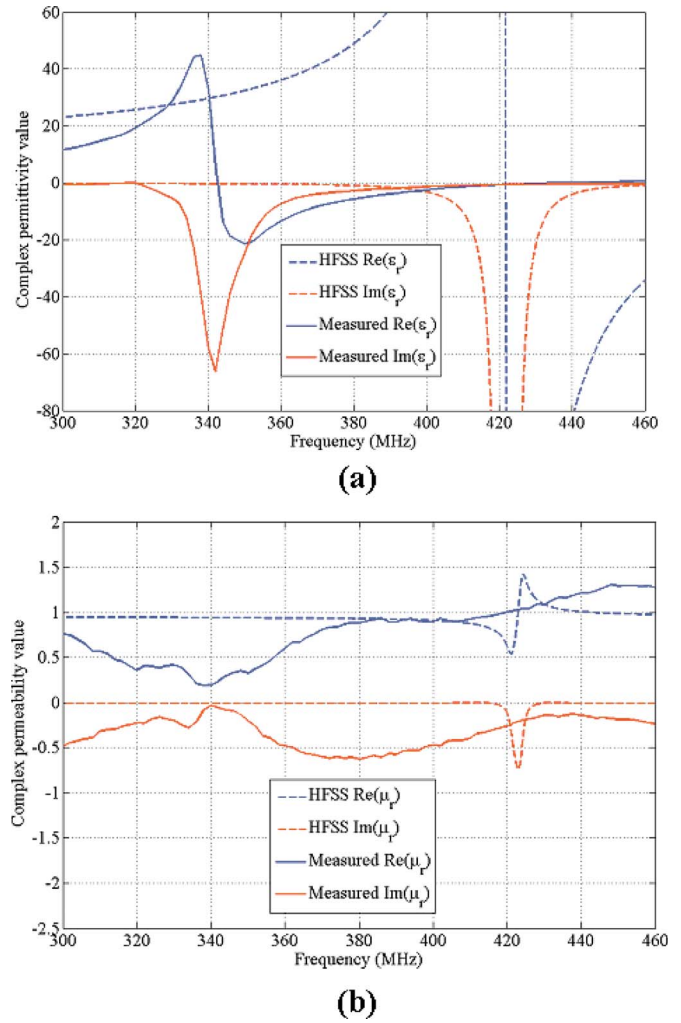

(a)

(b)

FIG. 10. (Color online) Measured and predicted complex effective relative (a) permittivity and (b) permeability values obtained for the ENG unit cell realization of NIM design 1. The predicted values were generated numerically using HFSS-only simulations.

are the smallest ones measured to date, with $\lambda_0 = 3 \times 10^{11}$ mm/s/340×10^6 Hz = 882.35 mm, and, hence $d \approx \lambda_0/88.24$.

With these results in hand, it was decided to try another HFSS-based modeling approach to achieve more accurate predictions of the resonance frequency in further design iterations. Instead of using the HFSS-provided RLC boundary condition, the S-parameters for the NIM unit cell were obtained first without the lumped elements being present. These S-parameters were then ported into Ansoft Designer, a circuit simulator. By introducing either an Ansoft Designer library lumped-element model or a manufacturer-measured lumped-element model into this circuit simulator, one can then predict the S-parameters of the entire system. The effective permittivity and permeability values were then extracted from these HFSS-Designer predicted S-parameters. Note that because circuit models of the actual lumped elements were not available, values for an ideal lumped-element included in the Ansoft Designer library, i.e., lossless lumped elements, were used for the HFSS-Designer simulations. The two numerical simulation approaches showed significantly different resonance characteristics. In particular, with identical unit cell
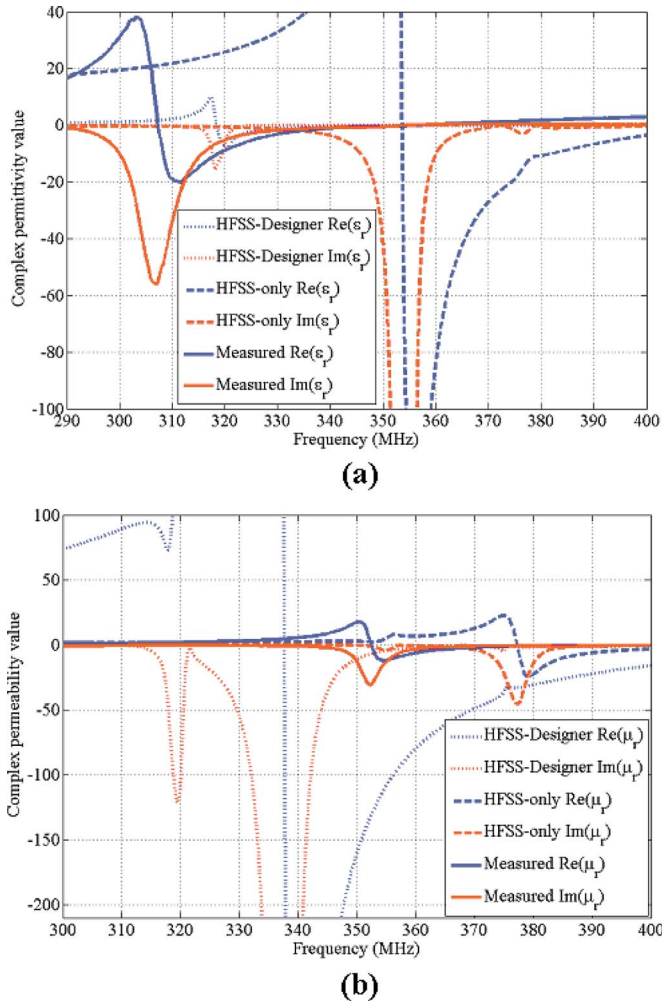
FIG. 11. (Color online) Measured and predicted complex effective relative (a) permittivity and (b) permeability values obtained for the NIM design 1 unit cell realization. The numerical values were generated using both HFSS-only and HFSS-Designer simulations.

design specifications, the HFSS-Designer approach predicted the resonance behaviors at lower frequencies, in better agreement with the measurements. To further investigate these issues, the structure was also modeled in the time domain using CST's MICROWAVE STUDIO. The CST simulations produced results that closely agreed with those obtained with the HFSS-Designer approach.

Comparisons of the numerically predicted and the measured effective relative permittivity and permeability values obtained for the NIM design 1 unit cell realization are given in Fig. 11. These effective values were extracted from the simulated or measured S-parameters, respectively. The resonant frequencies of the permittivity and permeability predicted by the HFSS-only simulations were 12% and 7%, respectively, different from the measured values. On the other hand, the HFSS-Designer simulation results in Fig. 11 clearly demonstrate a better estimate of the resonant frequency than the HFSS-only simulations yielded. In particular, the predicted permittivity and permeability resonant frequencies for the HFSS-Designer simulations were both 4% different from the measured values. These results suggested that it is possible to estimate correctly the resonance behavior roughly within the manufacturer's 5% tolerance on the lumped-element components used in the experiments.

Three subsequent NIM structures were designed (and fabricated) using the HFSS-Designer approach and/or CST MICROWAVE STUDIO simulations in order to more accurately achieve our desired goals. The HFSS-Designer simulations were generated using the capacitor model in the Panasonic measured S-parameter library to obtain more realistic dispersion properties, including losses. However, as for design 1, the Ansoft Designer ideal lumped element was used to model the inductor because the Panasonic library did not include the inductor values we used in the ENG structure. The 2D meanderline copper strips in the center of the dielectric were found to have a stronger impact on the negative-epsilon resonant behavior than the outer copper strips. Consequently, shorter spacings, E2 and S1, were used in the center of the ENG portion of the unit cell to obtain the desired resonant behavior with the minimum number of copper strips, which helped to minimize the copper losses in the meanderline.

Our fabricated finite NIM structures typically had a total of about 540 unit cells. Consequently, because of the associated computational requirements, it was not possible to use HFSS to simulate and accurately estimate the total losses in the fabricated NIM slab. Moreover, because there were so many lumped elements involved and with the indicated manufacturer tolerances on their values, there was a wide range in specific values associated with these unit cells. To obtain more realistic capacitance and inductance values for the capacitors and inductors to improve the numerical modeling, a total number of 20 random capacitors and inductors were chosen and measured at various UHF frequencies around 400 MHz. It was found that 5.6 pF was a good value for the capacitor, i.e., the measured capacitances were nearly frequency independent and very close to the manufacturer's advertised value. On the other hand, the manufacturer's advertised value of 470 nH for the inductor was specified at 10 MHz and data sheets indicated that its inductance increases in the UHF frequency regime of interest. Our measurements of the inductors indicated that their average inductance was 566 nH at 400 MHz.

With the above considerations taken into account, two improved NIM designs were fabricated and tested. The NIM design 2 proved that the simplified ENG portion of the unit cell was viable. The NIM design 3 considered small variations in the linewidths and separations, as well as the manufacturer specified and average measured values of the inductor. It achieved the design goal for the real part of the permittivity but with a 20% higher loss value than desired. With further tweaking of the design parameters based on comparisons of these designs and their experimental results, we obtained our final unit cell design, NIM design 4 shown in Fig. 12. It more precisely achieved the desired design goals.

The dimensions of the ENG and MNG portions of the NIM design 4 unit cell are summarized in Tables III and IV, respectively. The associated solder pad dimensions were again $a \times b = 1.1 \times 1.0$ mm². The total thickness along the x-axis was 2.542 mm. Thus, the overall NIM unit cell size was $2.542 \times 10 \times 10$ mm³. The fabricated NIM design 4 slab
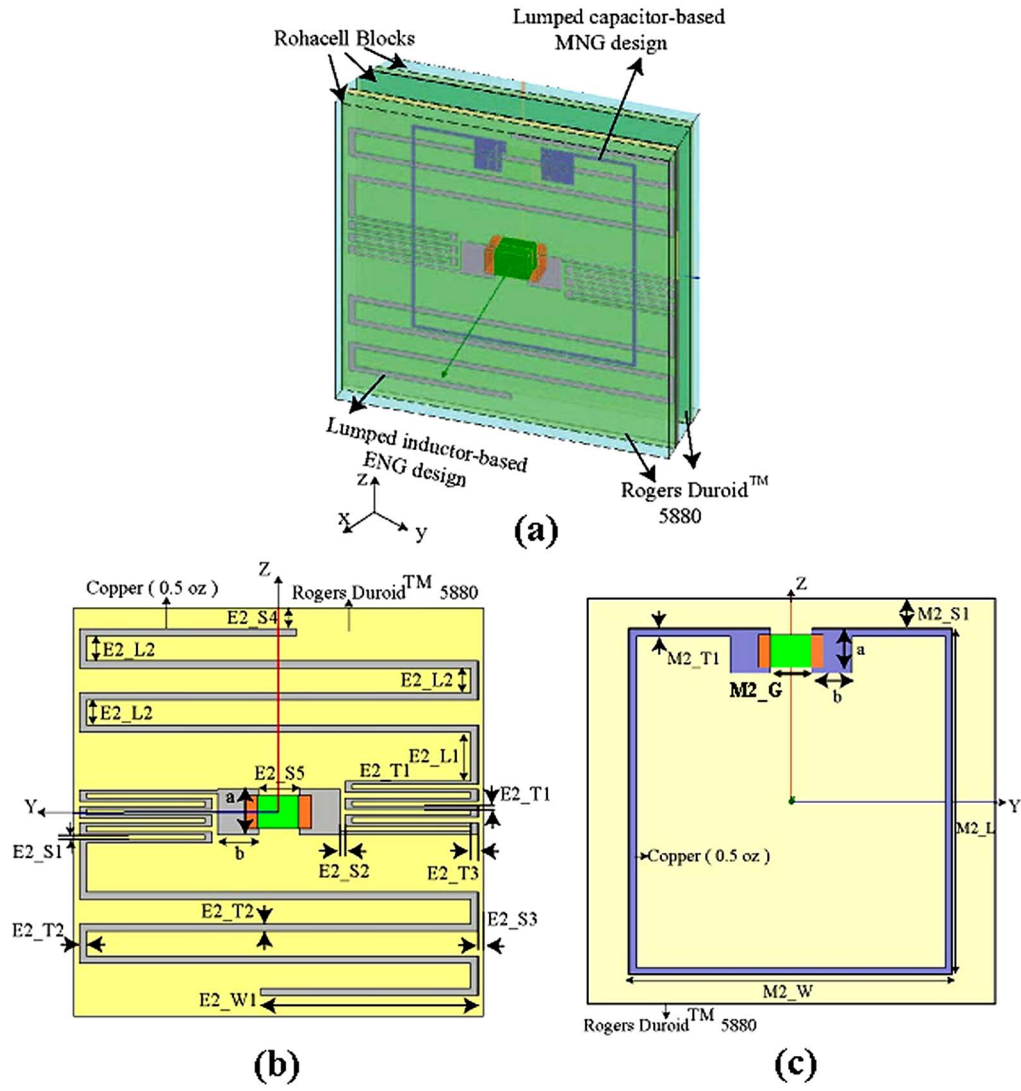
FIG. 12. (Color online) Detailed design specifications of the NIM design 4: (a) NIM unit cell, (b) ENG portion of the NIM unit cell based on a 2D meanderline integrated with a lumped-element inductor, and (c) MNG portion of the NIM unit cell based on a 2D rectangular loop integrated with a lumped-element capacitor.

TABLE III. Specifications of the ENG portion of the NIM design 4 unit cell

	E2_S1 (mm)	E_S2 (mm)	E2_S3 (mm)	E2_S4 (mm)	E2_S5 (mm)
	0.127	0.127	0.127	0.385	1.0
E2_T1 (mm)	E2_T2 (mm)	E2_T3 (mm)	E2_L1 (mm)	E2_L2 (mm)	E2_W1 (mm)
0.0762	0.1778	0.1778	1.1938	0.6096	5.3

TABLE IV. Specifications of the MNG portion and Rohacell™ thickness value of the NIM design 2 unit cell

M2_W(mm)	M2_L(mm)	M2_G(mm)	M2_T1(mm)	M2_S1(mm)	Rohacell™ thickness (mm)
6.476	6.572	1.0	1.746	1.577	1.1

was again three unit cells deep. As with the NIM design 1, the lumped elements were embedded into the Rohacell™ slab to minimize the NIM unit cell thickness.

This NIM design 4 was modeled using the CST MICRO-WAVE STUDIO simulator; it allowed the use of three unit cells in the direction parallel to the incident electric field, a configuration that was thought to be a slightly better match to the experimental boundary conditions. Comparisons of the one and three unit cell configurations showed little difference. Constant frequency values for the capacitor, 5.6 pF, and inductor, 470 nH, were employed. The NIM design 4 parameters were varied to achieve the effective index of refraction value $n_{\mathrm{real}} \approx -3.0$ at approximately 420 MHz. Again, this choice was made because the previous CST MICROWAVE STUDIO simulations all showed a +20 MHz shift in the simulated resonance frequencies when compared to the measurement values. The indicated inductor value was used in order to be consistent with those previous CST simulations. It was also assumed that any experimental errors (e.g., the lumped-element tolerances and fabrication errors) would be the same. Thus, the observed experimental-simulation frequency shift differences were also taken into account in the NIM design 4. The NIM design 4 slab was fabricated; it is shown in Fig. 6. It again consisted of three unit cells in the direction of propagation of the incident field. The numerical simulations, which accounted for the noted frequency offset, predicted the measured locations of the permittivity and permeability resonance dips with high accuracy, as shown in Fig. 13. The measured effective index of refraction results for the NIM design 4 slab are shown in Fig. 14(a) for the entire frequency band and in Fig. 14(b) for frequencies in the immediate neighborhood of the target frequency.

The loss was obtained in two ways. The first loss calculation was obtained from the extracted effective index of refraction as

$$\mathrm{Loss(dB/cm)} = -10 \log_{10}[\exp(-2.0 \\ \times 2\pi f \, \mathrm{Im}(n) d_{\mathrm{slab}}/c)]/d_{\mathrm{slab}}, \tag{1}$$

where d_{slab} is the thickness of the slab in cm. The calculated loss value was also obtained directly from the measured and predicted S-parameters as

$$\mathrm{Loss(dB/cm)} = -10 \log_{10}\left(\frac{|S_{21}|^2}{1 - |S_{11}|^2}\right)/d_{\mathrm{slab}}. \tag{2}$$

The agreement between the two approaches was excellent in all of the simulated and measured cases.

The fabricated NIM slab was shown to have an effective $n_{\mathrm{real}} = -3.11$ at 400 MHz with a 0.91 dB/cm loss value. The effective unit cell size was $d = \lambda_0/75$. Thus our design goals were met with this NIM design 4, as verified by these measurement results.

IV. CONCLUSIONS

We designed a lumped-element-based NIM MTM that had a unit cell size $d \sim \lambda_0/75$ at 400 MHz having losses less than 1.0 dB/cm and an effective index of refraction $n_{\mathrm{real}}(400\ \mathrm{MHz}) \approx -3.0$. Four design iterations were fabricated and measured. Comparisons of the measured and pre-
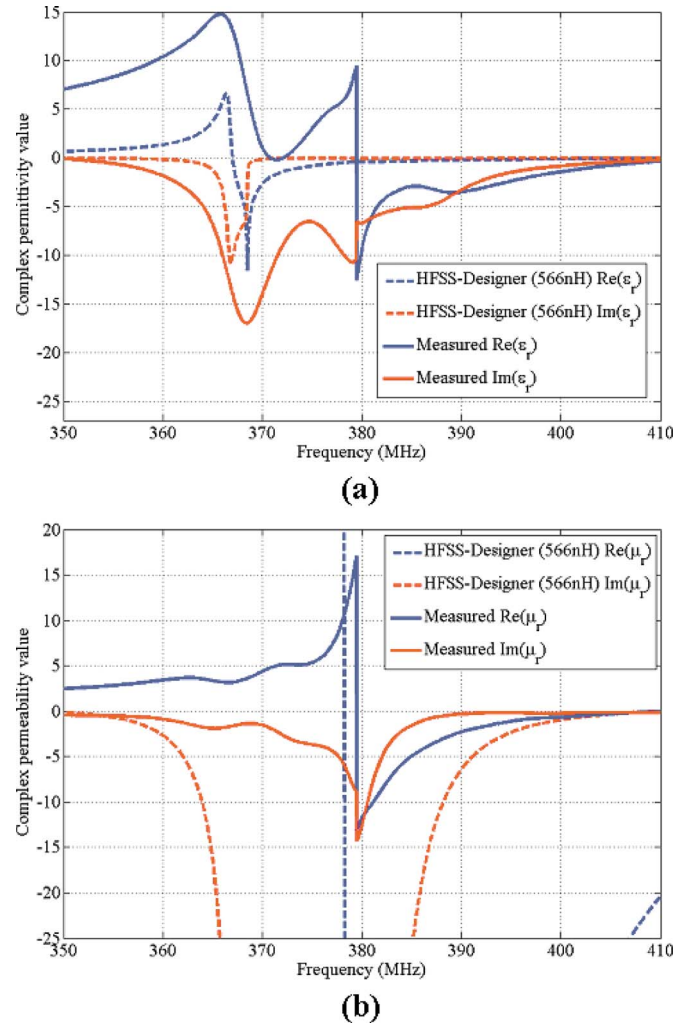

(a)

(b)

FIG. 13. (Color online) Measured and predicted complex effective relative (a) permittivity and (b) permeability values obtained for the NIM design 4 unit cell realization. The numerical values were generated with the HFSS-Designer approach. Note that the simulations predict the resonant frequencies of the effective ε_r and μ_r with high accuracy.

dicted results were presented for the initial and final designs. Favorable agreement between the predicted and experimental values was demonstrated. Because the NIM unit cell was constructed from an ENG and an MNG portion, an ENG-only slab was also fabricated. It produced effective negative permittivity values at lower frequencies than the NIM slabs, hence, with a smaller effective unit cell size. It also provided useful design information about the coupling effects between the MNG and ENG portions of the unit cell.

The initial measurements guided our choice to use a HFSS-Designer simulation approach to most accurately model the unit cells under consideration. It was determined that the CST MICROWAVE STUDIO simulations provided similar results. Both approaches, one in the frequency domain and one in the time domain, were able to handle the lumped elements more accurately than the HFSS-only approach. The final NIM design 4 was simulated using our standard frequency domain HFSS-Designer model as well as the time domain CST MICROWAVE STUDIO model. The CST MICROWAVE STUDIO predictions guided the fabrication and measurements of the
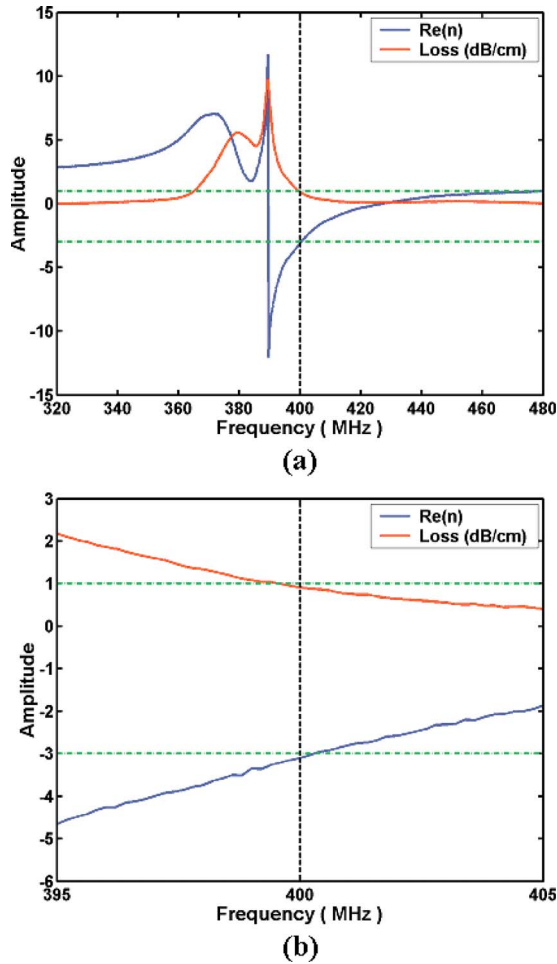
FIG. 14. (Color online) Measured effective index of refraction values obtained for the NIM design 4 unit cell structure: (a) entire measured frequency band and (b) zoom. Our goals were met with this design since at 400 MHz the measured real part of the effective refractive index $n_{\text{real}}=-3.11$ with a loss value of 0.91 dB/cm.

NIM design 4 slab which met the specified performance goals.

It is noted that the wave impedance of the slabs was calculated in all cases. However, it was not a major design goal to achieve a relative wave impedance value equal to 1, i.e., a slab wave impedance matched to the free-space wave impedance value. Nonetheless, in the final realization, NIM design 4, the measured relative impedance of the slab at 400 MHz was 0.756. This means the power accepted by the NIM slab was 98% of the incident power. Future designs could and should be achieved with the NIM slab matched to free space to maximize the power accepted by it.

It was found that the actual lumped-element capacitance and inductance values had a significant impact on the final NIM performance. Future efforts should include development of a frequency dependent model of the inductor to

achieve even more accurate simulation results. Higher quality components with lower parameter tolerances would enhance the comparisons of the simulation and experimental results. It was found that the majority of the losses in these designs originate in the lumped elements and in the very thin copper traces. It is believed that with improved components, even smaller loss, low frequency NIM materials can be fielded for a variety of practical applications.

ACKNOWLEDGMENTS

[1]N. Engheta and R. W. Ziolkowski, IEEE Trans. Microwave Theory Tech. **53**, 1535 (2005).
[2]*Metamaterials: Physics and Engineering Explorations*, edited by N. Engheta and R. W. Ziolkowski (IEEE, New York/Wiley, New York, 2006).
[3]D. R. Smith, W. J. Padilla, D. C. Vier, S. C. Nemat-Nasser, and S. Schultz, Phys. Rev. Lett. **84**, 4184 (2000).
[4]R. A. Shelby, D. R. Smith, S. C. Nemat-Nasser, and S. Schultz, Appl. Phys. Lett. **78**, 489 (2001).
[5]M. Bayindir, K. Aydin, E. Ozbay, P. Markoš, and C. M. Soukoulis, Appl. Phys. Lett. **81**, 120 (2002).
[6]K. Li, S. J. McLean, R. B. Greegor, C. G. Parazzoli, and M. Tanielian, Appl. Phys. Lett. **82**, 2535 (2003).
[7]C. G. Parazzoli, R. B. Greegor, K. Li, B. E. C. Koltenbac, and M. Tanielian, Phys. Rev. Lett. **90**, 107401 (2003).
[8]R. W. Ziolkowski, IEEE Trans. Antennas Propag. **51**, 1516 (2003).
[9]*Negative Refraction Metamaterials: Fundamental Properties and Applications*, edited by G. V. Eleftheriades and K. G. Balmain (IEEE, New York/Wiley, Hoboken, NJ, 2005).
[10]C. Caloz and T. Itoh, *Electromagnetic Metamaterials: Transmission Line Theory and Microwave Applications* (IEEE, New York/Wiley, New York, 2005).
[11]R. W. Ziolkowski and A. Erentok, IEEE Trans. Antennas Propag. **54**, 2113 (2006).
[12]R. W. Ziolkowski, and A. Erentok, IET Proc. Microwaves, Antennas Propag. **1**, 116 (2007).
[13]A. Erentok and R. W. Ziolkowski, IEEE Trans. Antennas Propag. **55**, 731 (2007).
[14]J. A. Gordon and R. W. Ziolkowski, Opt. Express **15**, 2622 (2007).
[15]P. Imhof, M.S. thesis, Ecole Polytechnique Federale de Lausanne, 2006.
[16]P. D. Imhof, R. W. Ziolkowski, and J. R. Mosig, Proceedings of the 2006 IEEE AP-S International Symposium and USNC/URSI National Radio Science Meeting, Albuquerque, NM, 9–14 July 2006.
[17]P. D. Imhof, R. W. Ziolkowski, and J. R. Mosig, *Proceedings of the European Conference on Antennas and Propagation, EuCAP2006* (European Space Agency, Noordwijk, The Netherlands, 2006).
[18]R. B. Greegor, C. G. Parazzoli, J. A. Nielsen, M. A. Thompson, M. H. Tanielian, D. C. Vier, S. Schultz, D. R. Smith, and D. Schurig, IET Proc. Microwaves, Antennas Propag. **1**, 108 (2007).
[19]S. A. Cummer and B.-I. Popa, Appl. Phys. Lett. **85**, 4564 (2004).
[20]H. Chen, J. Zhang, Y. Bai, Y. Luo, L. Ran, Q. Jiang, and J. A. Kong, Opt. Express **14**, 12944 (2006).
[21]D. R. Smith, S. Schultz, P. Markos, and C. M. Soukoulis, Phys. Rev. B **65**, 195104 (2002).
[22]R. W. Ziolkowski and F. Auzanneau, J. Appl. Phys. **82**, 3195 (1997).
[23]R. W. Ziolkowski and F. Auzanneau, J. Appl. Phys. **82**, 3192 (1997).
[24]F. Auzanneau and R. W. Ziolkowski, J. Phys. III **7**, 2405 (1997).
[25]A. Erentok, P. Luljak, and R. W. Ziolkowski, IEEE Trans. Antennas Propag. **53**, 160 (2005).